AD-A209 249

Technical Report 1271
February 1989

Apparent Infrared Radiance of the Sea

H. G. Hughes

Approved for public release; distribution is unlimited.

89 6 20 244

NAVAL OCEAN SYSTEMS CENTER
San Diego, California 92152-5000

ADMINISTRATIVE INFORMATION

ACKNOWLEDGMENTS

JG

REPORT DOCUMENTATION PAGE

1a. REPORT SECURITY CLASSIFICATION UNCLASSIFIED		1b. RESTRICTIVE MARKINGS
2a. SECURITY CLASSIFICATION AUTHORITY		3. DISTRIBUTION/AVAILABILITY OF REPORT
2b. DECLASSIFICATION/DOWNGRADING SCHEDULE		Approved for public release; distribution is unlimited.
4. PERFORMING ORGANIZATION REPORT NUMBER(S) Technical Report 1271		5. MONITORING ORGANIZATION REPORT NUMBER(S)

6a. NAME OF PERFORMING ORGANIZATION Naval Ocean Systems Center	6b. OFFICE SYMBOL (If applicable) Code 543	7a. NAME OF MONITORING ORGANIZATION
6c. ADDRESS (City, State and ZIP Code) San Diego, California 92152–5000		7b. ADDRESS (City, State and ZIP Code)
8a. NAME OF FUNDING/SPONSORING ORGANIZATION Office of Naval Technology	8b. OFFICE SYMBOL (If applicable)	9. PROCUREMENT INSTRUMENT IDENTIFICATION NUMBER

8c. ADDRESS (City, State and ZIP Code) Arlington, VA 22217-5000	10. SOURCE OF FUNDING NUMBERS			
	PROGRAM ELEMENT NO.	PROJECT NO.	TASK NO.	AGENCY ACCESSION NO.
	62435N	RA35G80/ RU35G80	NO1A	DN888 715

11. TITLE (include Security Classification)

APPARENT INFRARED RADIANCE OF THE SEA

12. PERSONAL AUTHOR(S)

H. G. Hughes

13a. TYPE OF REPORT Interim	13b. TIME COVERED FROM Sep 1988 TO Nov 1988	14. DATE OF REPORT (Year, Month, Day) February 1989	15. PAGE COUNT 21

16. SUPPLEMENTARY NOTATION

17. COSATI CODES			18. SUBJECT TERMS (Continue on reverse if necessary and identify by block number)
FIELD	GROUP	SUB–GROUP	Advanced Very High Resolution Radiometer (AVHRR) Forward Looking Infrared (FLIR)

19. ABSTRACT (Continue on reverse if necessary and identify by block number)

In this report, the relative contributions of sky radiance reflections and emissions from the sea surface and the intervening atmosphere are examined as a function of sensor altitude. Calculations of the apparent sea radiance as a function of zenith angle were made using a modified version of LOWTRAN 6. The calculations showed the emissions of the intervening atmosphere to be the major contributor to the apparent sea radiance received at higher elevations from zenith angles within a few degrees of the horizon.

20. DISTRIBUTION/AVAILABILITY OF ABSTRACT ☐ UNCLASSIFIED/UNLIMITED ☒ SAME AS RPT ☐ DTIC USERS	21. ABSTRACT SECURITY CLASSIFICATION UNCLASSIFIED	
22a. NAME OF RESPONSIBLE INDIVIDUAL H. G. Hughes	22b. TELEPHONE (Include Area Code) (619) 553–1418	22c. OFFICE SYMBOL Code 543
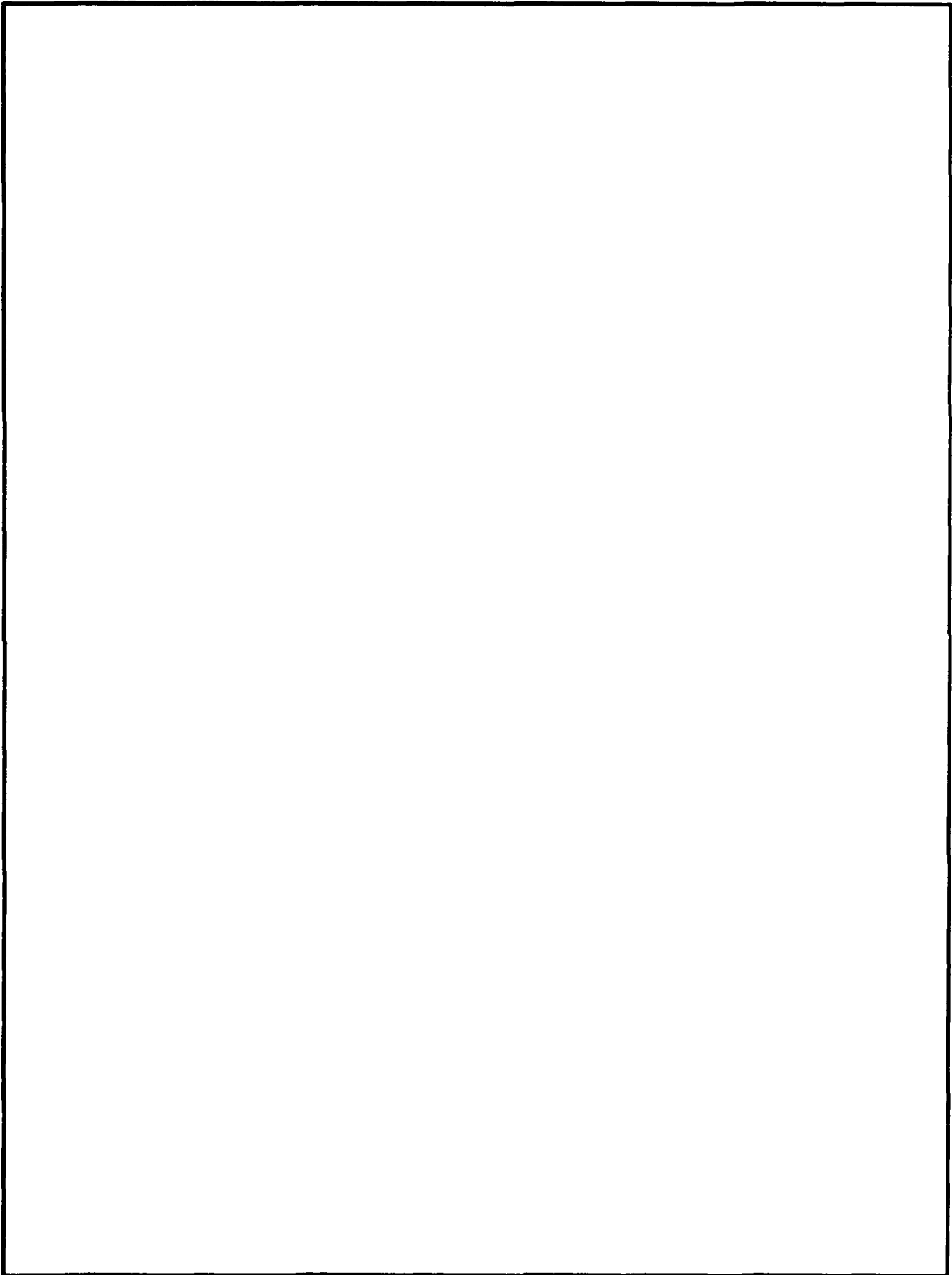
DD FORM 1473, 84 JAN

83 APR EDITION MAY BE USED UNTIL EXHAUSTED
ALL OTHER EDITIONS ARE OBSOLETE

SUMMARY

Near-surface measurements of infrared (8 to 12 μm) horizon radiances are presented for 2 days with differing surface wind speed conditions and vertical profiles of meteorological parameters. A representative aerosol size distribution model for each day was chosen which allowed calculations using LOWTRAN 6 (Kneizys, et al., 1983) to best match the measured horizon pixel radiance and the atmospheric optical depths determined from the upwelling solar radiances detected by Channel 1 (0.58 to 0.65 μm) of the Advanced Very High Resolution Radiometer (AVHRR) on board the National Oceanic and Atmospheric Administration (NOAA)-9 satellite.

The selected models were then used in calculations of the apparent sea surface radiance as a function of zenith angle using a modified version of LOWTRAN 6 (Wollenweber, 1988). This program incorporates a statistical wave slope model (Cox and Munk, 1954) to account for the contributions to the apparent sea radiance from sky reflections and emissions from the surface wave facets and atmospheric path. Good agreement between calculated sea radiances and those measured at an altitude of 33 m was obtained within 1° of the horizon for low and moderate surface wind speeds.

Using these models, the relative contributions of the three components to radiances received at different altitudes from other zenith angles were determined. The calculations showed the emission of the intervening atmosphere to be the major contributor to the apparent sea radiance received at higher elevations from zenith angles within a few degrees of the horizon. The resulting variations of apparent temperature of the sea surface with zenith angle were also found to be strongly dependent on the vertical profiles of air temperature.

i

CONTENTS

FIGURES

FIGURES (cont'd.)

INTRODUCTION

To be of practical use in tactical situations, airborne Forward Looking Infrared (FLIR) systems must be able to detect a surface target at ranges of several tens of kilometers. This requirement limits the depression viewing angles to within a few degrees of the horizontal. As an example, the range to a target as viewed with a 1° depression angle is 80 km for an airborne FLIR operating at an altitude of 1 km. Depressing the viewing angle another 2° places the target only 20 km away. To predict the FLIR's performance, the spectral radiance contrast between the target and the sea background is required. The performance range is determined to be that range where the difference between the apparent ship's temperature (i.e., the actual ship temperature degraded by the atmospheric transmittance) and the effective background temperature of the sea is equal to the minimum detectable temperature difference (detection) or the minimum resolvable temperature difference (identification and classification) of the FLIR system. For the larger viewing angles, the infrared (IR) radiance of the sea surface is the primary contributor to the background scene. Closer to the horizon, however, the sky radiance reflections and emissions by the intervening atmosphere must be taken into account. While a smooth sea is a poor emitter of IR at the small viewing angles, emissions from the individual wave facets of a wind-ruffled sea contribute to the background scene.

In this report, the relative contributions of sky radiance reflections and the emissions from the sea surface and the intervening atmosphere are examined as a function of sensor altitude. For these calculations, airborne measurements of the vertical profiles of meteorological parameters and sea surface temperatures, obtained on 2 days during low and moderate wind speed conditions, are used as inputs to a modified version of LOWTRAN 6 (Wollenweber, 1988). In addition to the path emissions, this version incorporates the Gaussian distributed wave slope model of Cox and Munk (1954) to calculate the contributions from sky radiance reflections and the emissions from a wind-ruffled sea surface. In the following sections, the mathematical formulation of the background radiance scenes are presented. A technique is also discussed by which low-level measurements of horizon IR radiances were used with visible upwelling solar radiances (as detected by the National Oceanic and Atmospheric Administration (NOAA)-9 Advanced Very High Resolution Radiometer (AVHRR) to select the appropriate LOWTRAN 6 aerosol size distribution parameters for the radiance calculations. The measured horizon radiances were also used to test the atmospheric models used in the radiance calculations with altitude.

MATHEMATICAL FORMULATION OF BACKGROUNDS

Consider the atmosphere to be composed of a number, N, of isothermal layers characterized by temperature T_i and transmittance $\tau(v,i,\mu)$ along the optical path traversing the ith layer at angle μ, and v is the spectral wave number. From Kirchoff's law, the radiance of the ith layer is

$$N(v,i,\mu)_{sk} = [1 - \tau_a(v,i,\mu)]W(T_i)/\pi \qquad (1)$$

1

where $\tau_a(v,i,\mu)$ is the absorption transmittance and $W(T_i)$ is Planck's blackbody radiation formula. Then the spectral radiance reaching the sea surface through the intervening atmosphere is

$$N(v,i,\mu)_{sk}[\prod_{j=1}^{i-1}\tau(v,j,\mu)] = [1-\tau_a(v,i,\mu)][\prod_{j=1}^{i-1}\tau(v,j,\mu)]W(\bar{T_i})/\pi. \qquad (2)$$

Summing the contribution from all layers, the spectral radiance at the sea surface is then

$$N(v,\mu)_{sk} = [\sum_{i=1}^{n}[1-\tau_a(v,i,\mu)][,i,\mu)][\prod_{j=1}^{i-1}\tau(v,j,\mu)]W(T_i)/\pi. \qquad (3)$$

As shown in figure 1, the radiance is allowed to strike a wave facet on the ocean surface with a Gaussian distribution (Cox and Munk, 1954) of angular tilts α and β in the upwind and crosswind directions, respectively, such that an amount $N(v,\mu)'$ is reflected into the sensor at an altitude H_1 within the mth layer. The probability that radiance hits the facet is equal to the probability that the wave slope exist, i.e.,

$$N(v,\mu)' = P(S_x, S_y)N(v,\mu)_{sk} \qquad (4)$$

where

$$P(S_x, S_y) = 1/(2\sigma_x\sigma_y)EXP[0.05(S_x^2/\sigma_x^2 + S_y^2/\sigma_y^2)] \qquad (5)$$

and $S_x = \tan\alpha$, $S_y = \tan\beta$, $\sigma_x^2 = 0.003 + 1.92\times10^3 V_c$, $\sigma_y^2 = 3.16\times10^3 V_c$, with V_c being equal to the current wind speed in the azimuthal direction ϕ with respect to the sensor. Then, the total spectral radiance reflected from all the wave facets into the line of sight of the detector located in the mth layer is

$$N(v,\theta)_{rsk} = [\prod_{j=1}^{m-1}\tau(j,\theta)]\Sigma R(v,\Omega)P(S_x, S_y N(v,\mu)_{rsk}) \qquad (6)$$

where $R(v,\Omega)$ is the complex reflectivity of sea water at the reflection angle Ω. In the above equations, both μ and Ω are implicit functions of S_x nd S_y given by (Wollenweber, 1988)

$$\cos\mu = (2S_x/A)\cos\theta'\cos\phi + (2S_y/A)\cos\theta'\cos\phi - (B/A)\sin\theta' \qquad (7)$$

$$\cos\Omega = (2S_x/A)\cos\theta'\cos\phi + (S_y/A)\cos\theta'\cos\phi + (1/A)\sin\theta' \qquad (8)$$

where $A = S_x^2 + S_y^2 + 1$, $B = S_x^2 + S_y^2 - 1$ and θ' is the sensor's zenith angle at the sea-surface reflection point.
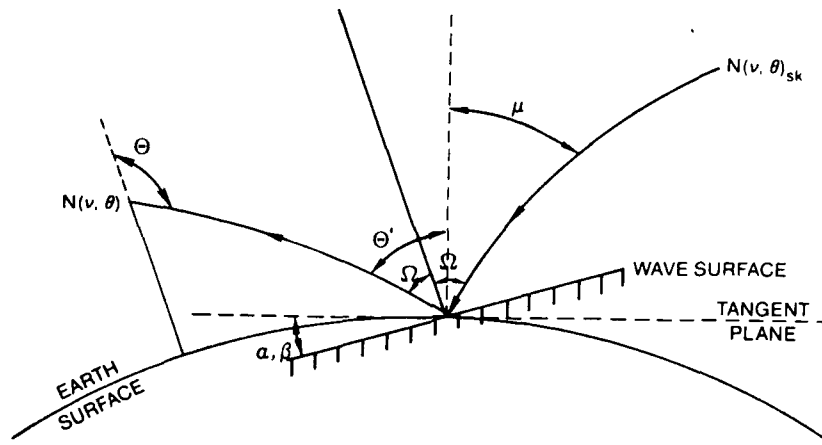
Figure 1. Reflection geometry from a wind-ruffled sea surface.

Similarly, the spectral radiances emitted by the sea-surface wave facets (N_{ss}) and the path radiance (N_p), which reach the sensor at the zenith angle θ, are given by

$$N(v, \theta)_{ss} = [\prod_{j=1}^{m-1} \tau(v, j, \theta)] \sum_{\Omega} P(S_x, S_y)[1 - R(v, \Omega)]W(T_{ss})/\pi \qquad (9)$$

and

$$N(v, \theta)_p = [\sum_{i=1}^{m} [1 - \tau_a(v, i, \theta)][\prod_{j=i+1}^{m-1} \tau(v, j, \theta)]W(T_i)/\pi \qquad (10)$$

where T_{ss} is the sea-surface temperature, and again, the angle μ is implicit in the reflection angle Ω.

Then, the total spectral radiance reaching the detector is the sum of the three components

$$N(v, \theta)_{tot} = N(v, \theta)_{rsk} + N(v, \theta)_{ss} + N(v, \theta)_p. \qquad (11)$$

The total spectral radiance must then be averaged over the response of the FLIR system, which in this case is taken to be the 8- to 12-μm wavelength band. Subroutines have been introduced into LOWTRAN 6 (Wollenweber, 1988) to calculate the total band averaged radiance. The reflection and zenith angles are calculated with equations 5, 7, and 8 corresponding to the incremented values of wave slopes in the intervals $-3\sigma_{x,y} < S_{x,y} < 3\sigma_{x,y}$. To limit the number of calculations, the zenith angles are divided into a maximum of 30 classes (with the criterion that each class should contain at least 10 percent of the probability), and the averaged angles for each class are then used in the radiance calculations.

MEASUREMENTS AND AEROSOL MODEL SELECTION

For this study, a Piper Navajo aircraft, equipped with Rosemount temperature and pressure probes and an EG&G dewpoint sensor, made vertical spirals over the ocean to obtain the profile of temperature, relative humidity, and pressure which are required inputs to the LOWTRAN 6 computer code for calculating the sea and sky radiances. A Barnes PRT-5 radiation thermometer was also on board the aircraft for measurement of the sea-surface temperatures from low-level, constant-altitude flights. The vertical profiles of temperature and relative humidity, measured at 1440 PST on 29 September and 25 November 1988 off the coast of San Diego, California, are shown in figures 2 and 3 respectively. The measured sea-surface temperatures were 15.2°C on 29 September and 17.6°C on 25 November. At the time the meteorological parameters were obtained, measurements of IR (8 to 12 μm) horizon radiances were also made with a calibrated thermal imaging system (AGA THERMOVISION, model 780) using a 2.95° field-of-view lens with an instantaneous field of view of 0.87 mr. The response of the system was determined by placing a blackbody of known temperature ($\pm$0.1°C for temperatures <50°C) in front of the lens aperture. The digitized video signal transfer function of the system then allowed the blackbody temperature to be reproduced to within $\pm$0 2°C. For these measurements, the scanner was located at an elevation of 33 m on the Point Loma peninsula in San Diego and was directed due west over the ocean such that approximately half of the field of view was above and half below the horizon. The measured radiance scenes are shown in figure 4. The temperatures of the different colors in each scene are also identified by the color bars displayed on the left which correspond to the midpoints of the temperatures printed above and below each bar. The data processing software of the AGA system also allows the vertical profile of the effective blackbody temperature in the scene to be displayed on the right side of the thermogram. In each scene, the horizontal cursor is situated on the pixel corresponding to the maximum temperature (20.4°C or 3.46 mW/cm² sr and 16.5°C or 3.23 mW/cm² sr) which is taken to coincide with the infrared horizon. The increase is temperature with altitude (decreasing zenith angle) in the 29 September scene reflects the increase in air temperature with altitude shown in the figure 2. Similarly, the decrease in temperature with altitude in the 25 November scene can be related to the decrease in air temperature with altitude. The larger sky radiance values on 29 September may also partially result from the lower relative humidity above 200 m (figure 3), which decreased the number of activated aerosols available to scatter the radiation.

These measurements can be modeled with LOWTRAN 6 calculations to aid in selecting an appropriate aerosol model for radiance calculations on each day. The LOWTRAN 6 aerosol model chosen for the calculations is the Navy Maritime Aerosol Model. This model is the sum of three lognormal size distributions and, in addition to the surface wind speeds (current and 24 h averaged) and relative humidity, requires the input of an air mass factor which identifies the origin of the aerosols as either marine or continental and is allowed to range between integer values of 1 for open ocean to 10 for coastal regions. Also, when an accurate surface visibility is available as an input, the model is adjusted so that the calculated visibility at a wavelength of 0.55 μm is the same as the observed value. The air mass factor is defined in terms of atmospheric radon content or an air mass trajectory analysis to determine the time the air mass has been over land. As neither of these techniques was available, an alternate method was used to select an appropriate air mass factor. Using the current
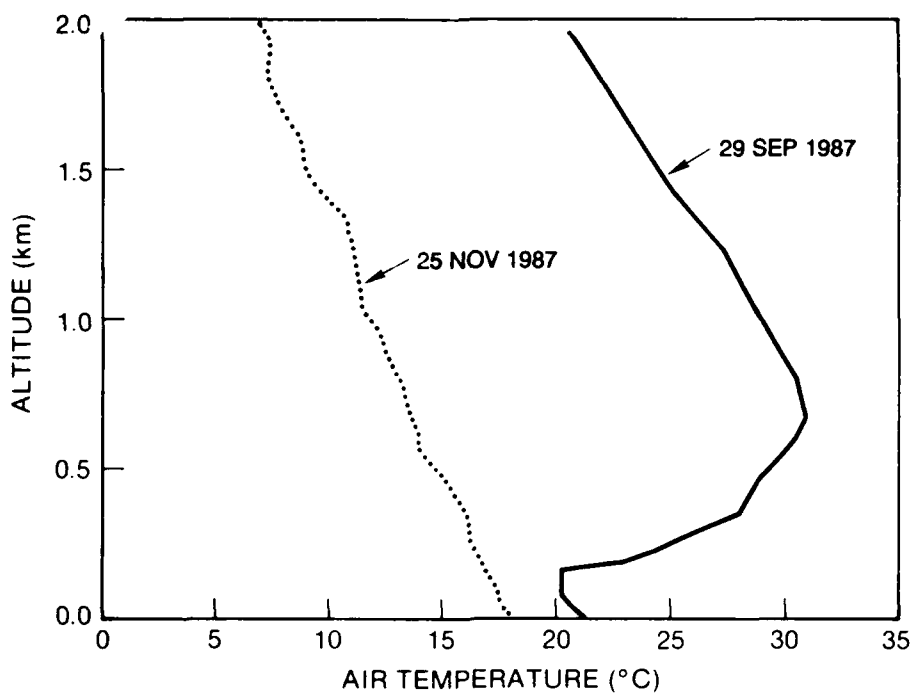
Figure 2. Profiles of air temperature measured with altitude on 29 September and 25 November 1987 off the coast of San Diego.
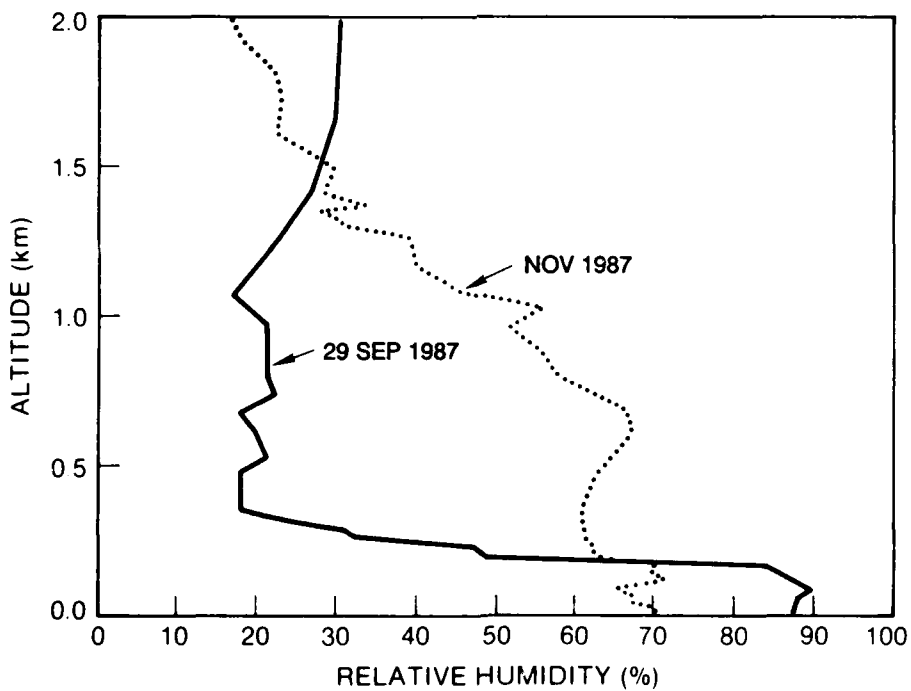

Figure 3. Profiles of relative humidity measured with altitude on 29 September and 25 November 1987 off the coast of San Diego.
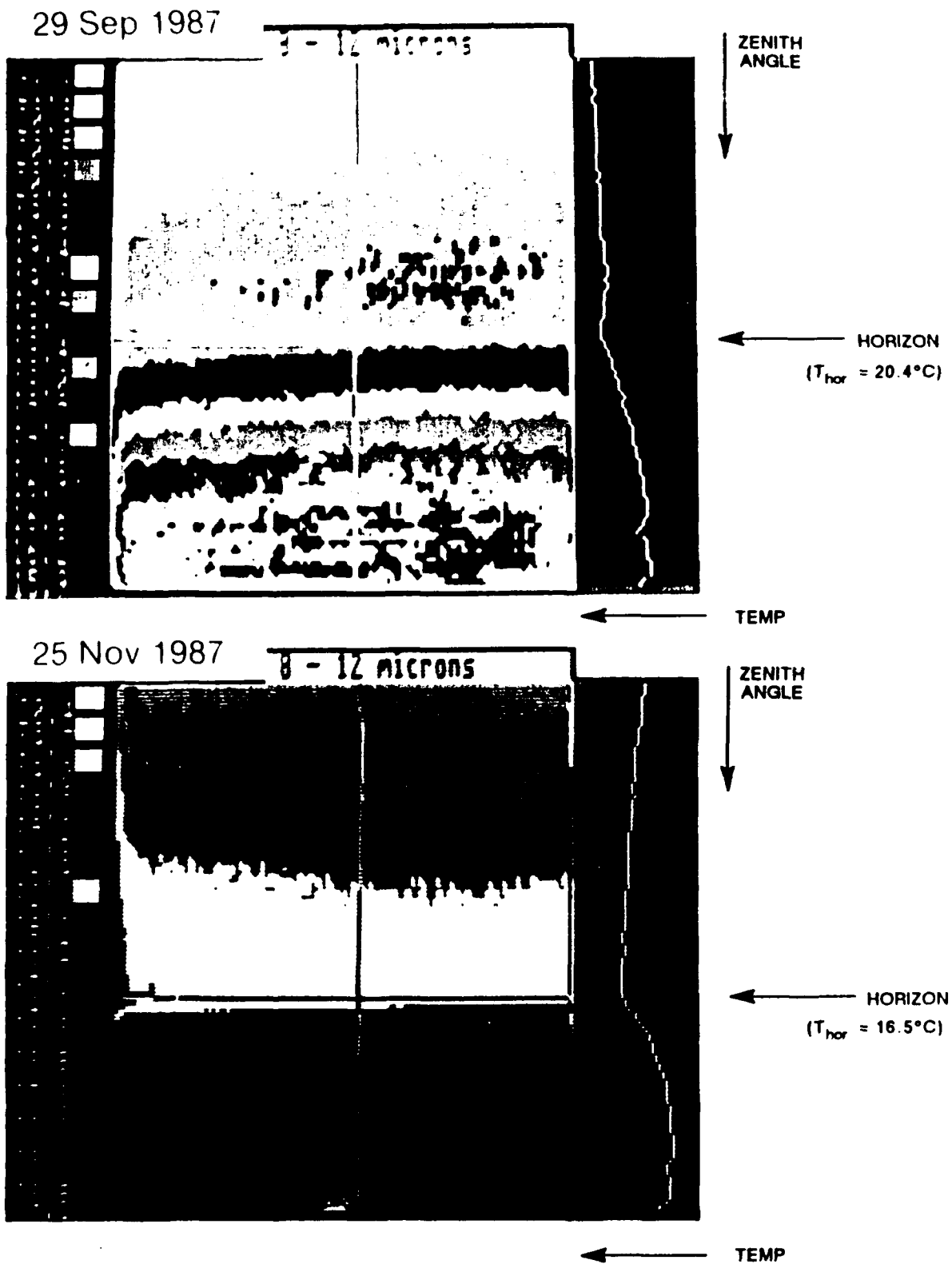
5

Figure 4. Thermogram of near horizon infrared (8 to 12 μm) radiances measured over the ocean by an AGA THERMOVISION Model 780 thermal imaging system on 29 September and 25 November 1987.

7

and 24-h averaged wind speeds (V_c = 7.5 m/s and $\overline{V}$ = 4.4 m/s for 29 September and V_c = 2.5 m/s and $\overline{V}$ = 3.9 m/s for 25 November) measured on shore at the AGA site and the vertical profiles of meteorological parameters, LOWTRAN 6 calculations were made to agree with the maximum pixel radiance in the scene using nonunique combinations of air mass factors and visibilities. In these calculations the meteorological profiles were divided into 33 layers as allowed by LOWTRAN 6. The lower layers of the profiles are also divided into sublayers containing the same amount of absorbing and scattering material and the temperature as the original layer. This artificial layering has been found necessary (Wollenweber, 1988) to remove the anomolous dip (Hughes, 1987) which occurs when aerosols are included in the LOWTRAN 6 radiance calculations for zenith angles close to 90°. As the AGA scanner could not be accurately plumbed, the zenith angle of the infrared horizon was taken be 0.01° less than the angle for which the LOWTRAN calculations indicated the refracted ray path first hit the earth. In these cases, the zenith angle corresponding to maximum radiance is 90.17°. In figure 5, the solid lines represent the locus of points which allow the LOWTRAN calculations to match the measured horizon pixel radiances with the different combinations of air mass factors and visibilities. Note that these calculations were made using a modified current wind speed component, $A_3 = 10^{(0.06 V_c - 2.8)}$, which is different from the value published in LOWTRAN 6. This modification was necessary to match previously published measurements of IR sky radiances and near-surface aerosol size distributions (Hughes, 1987) using the model.
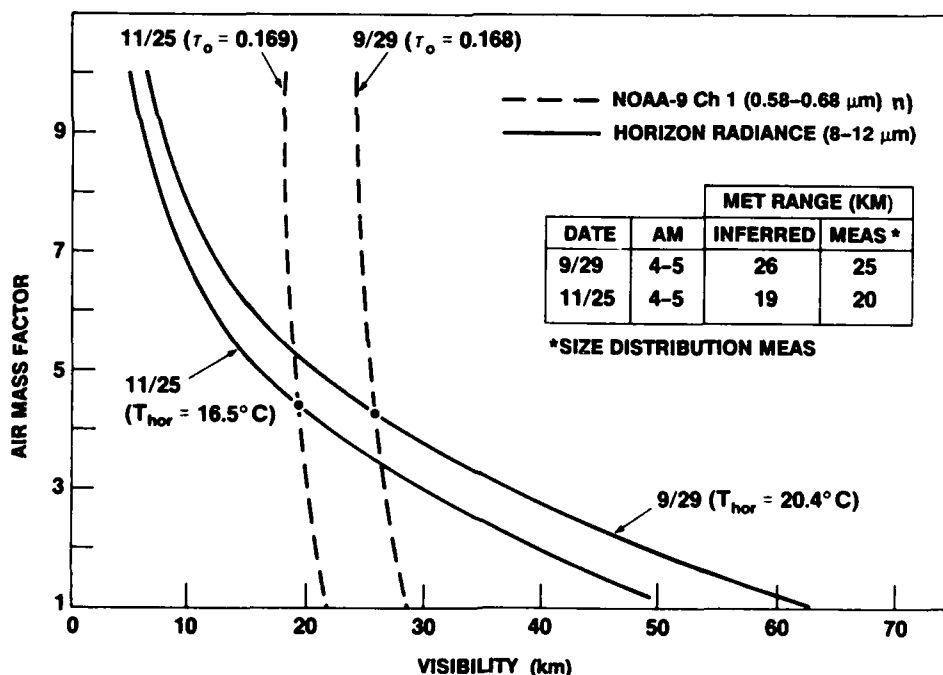

Figure 5. Loci of points of LOWTRAN 6 calculations with different combinations of air mass factors and visibilities which match measured values of IR horizon radiances (solid lines) and satellite detected visible optical depths (dashed lines) for 29 September and 25 November 1987.

At the time of the IR radiance measurements, upwelling solar radiances, detected by Channel 1 (0.58–0.65 μm) of the AVHRR on board the NOAA-9 satellite as it passed close to San Diego, were used to determine the total atmospheric optical depths (τ_o). They were determined using the SAIC (Science Applications International Corp.) satellite radiance computer code, which makes use of a direct linear relationship between upwelling radiance and the total atmospheric optical depth (Griggs, 1975). Although the vertical structure of the meteorological parameters which control aerosol growth were different, the total optical depths for the 2 days were nearly identical. In a manner similar to the IR radiance calculations, calculations of total atmospheric optical depth were made to agree with the measurements on both days. In these cases, the optical depths were calculated assuming all the aerosols to be confined to the mixed boundary layer as determined by the aircraft flights. The calculations of optical depths with different combinations of air mass factor and visibility are also shown in figure 5 as the dashed lines. The intersections of the solid and dashed lines then determine the best combinations of air mass factors and visibilities to be used in the background calculations. The inset in the figure shows the good agreement between the inferred visibilities and those calculated using aerosol size distributions measured at the lowest levels of the aircraft flights. These visibilities seem reasonable since Los Coronados Islands, located between 25 and 30 km off the coast of San Diego, were not visible to the naked eye on either day.

CALCULATION OF BACKGROUND RADIANCE SCENES

Figures 6 and 7 show the comparison of the measured and calculated IR radiances for zenith angles within about 1° below the horizon using the air mass factors and visibilities determined for the 2 days in figure 5. In both cases, the major contributor to the total radiance just below the horizon is the path emission. While the reflected sky radiance and the surface emission are small, their contribution to the total radiance at this low level (33 m) of observation cannot be neglected. It is interesting to note only a small reversal of the relative magnitudes of the reflected sky radiances and surface emissions between the two sets of calculations, which demonstrates the small influence of the wave slopes for the moderate wind speeds on 29 September. Both the calculated and measured total radiances on both days are in good agreement, which places confidence in their usefulness with radiance calculations at other altitudes and zenith angles.

Using the selected aerosol models, the contributions of the path, sea, and reflected sky radiances to the total background radiance were calculated as a function altitude and zenith angle. In figures 8 and 9, examples are presented of calculations for both days with a sensor altitude of 1000 m. For zenith angles less than about 95°, the major contribution to the background is the path emission with the reflected sky radiance being less than 10 percent of the total in both cases. In figure 10, the resulting apparent blackbody temperatures of the sea versus zenith angles for both days are compared. Again, the higher apparent temperature for zenith angles near the horizon on 29 September results from the path emission from the warmer elevated layers. The rapid falloff of path emission with increasing zenith angle (i.e., shorter slant paths to earth) is the cause of the decrease in apparent temperature on this day. In contrast, the temperature increase on 25 November is the result of the increase in emission from the warmer sea surface with increasing zenith angles. The relative contributions of the three components will, of course, change for other altitudes. Apparent sea
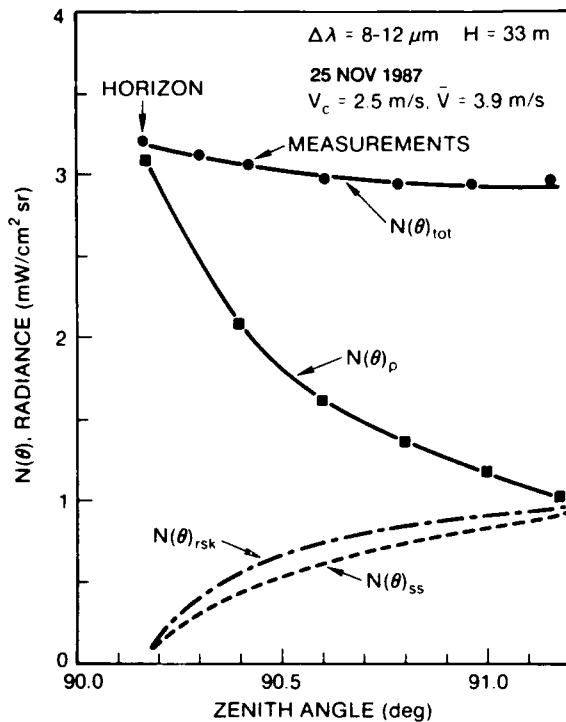
Figure 6. Comparison of the measured and calculated IR radiances for zenith angles about 1° below the horizon using the air mass factors and visibilities determined for 25 November 1987 in figure 5.
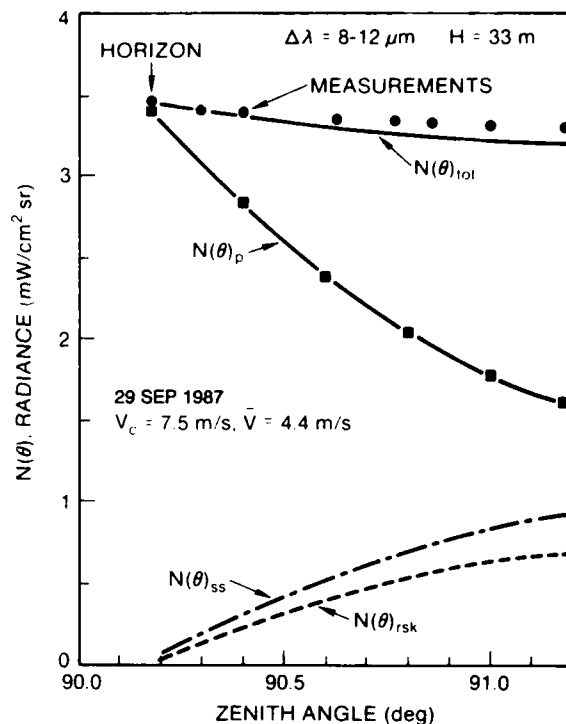
Figure 7. Comparison of the measured and calculated IR radiances for zenith angles about 1° below the horizon using the air mass factors and visibilities determined for 29 September 1987 in figure 5.

temperatures versus zenith angles calculated for sensor altitudes of 200 m, 500 m, and 1000 m are compared for each day in figures 11 and 12. The major differences occur on 29 September close to the horizon where, at a zenith angle of 92°, the apparent sea temperatures at 200 m and 1000 m differ by as much as 6°C. Smaller differences in temperature ($\approx$2°C) occur near this zenith angle on 25 November. As the nadir zenith angle is approached, the apparent temperatures at each altitude closely approach the measured sea surface temperature.

DISCUSSION

The results of this study have shown that the apparent background temperature of the sea surface varies with the altitude and viewing angle of the sensor. It is also strongly dependent upon the vertical profiles of temperature and relative humidity and the actual surface temperature. The primary contributor to the background scene for viewing angles close to the horizon is the emission of the intervening atmosphere. For the wind conditions examined here, however, there was little difference in the surface roughness effects.

The maximum detectable range of a FLIR system is usually defined as that range where the actual temperature difference between a target and its background ($T_t - T_b$) is degraded by the atmospheric transmittance, $\tau(R)$, to an apparent temperature difference, ΔT_a, equal to the minimum detectable temperature difference of the system. This approach neglects the changing background scene with sensor
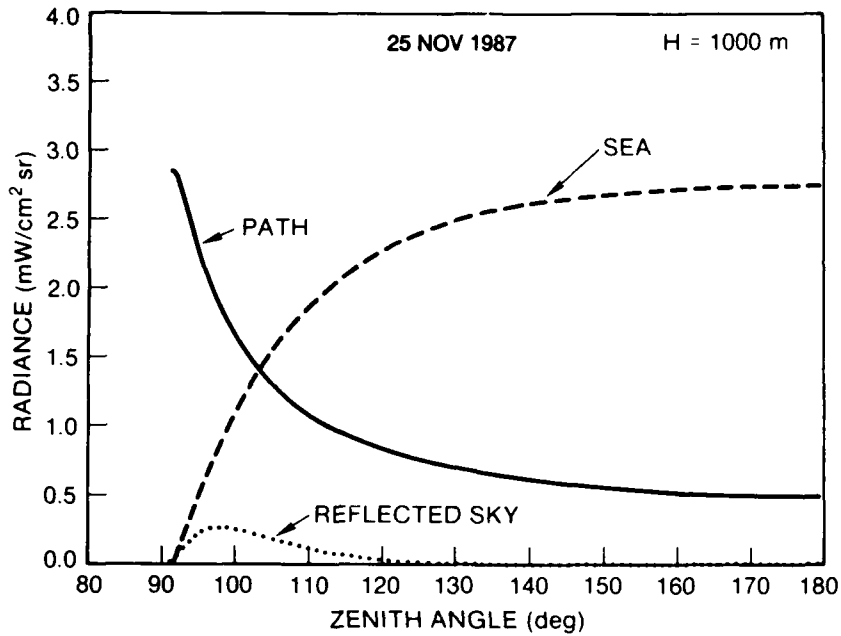
11

Figure 8. Calculations of contributions of the path, sea, and reflected sky radiances to the total background radiance as a function of zenith angle as viewed from an altitude of 1000 m on 25 November 1987.
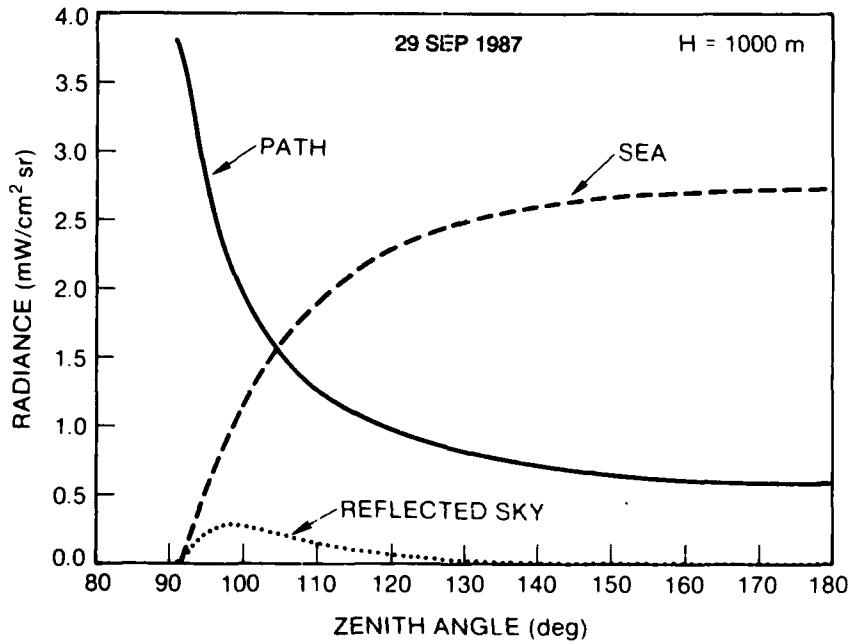

Figure 9. Calculations of contributions of the path, sea, and reflected sky radiances to the total background radiance as a function of zenith angle as viewed from an altitude of 1000 m on 29 September 1987.
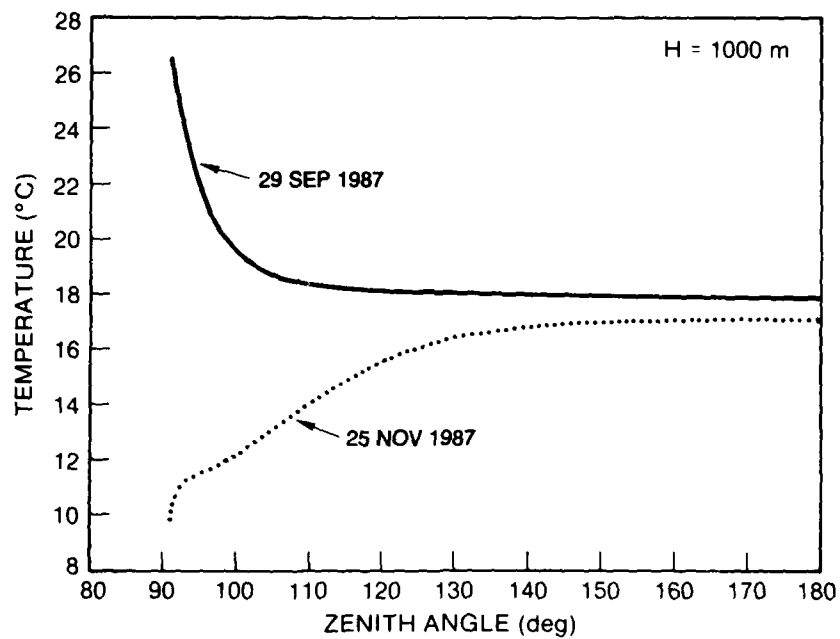
12

Figure 10. Calculations of the apparent blackbody temperature of the sea versus zenith angle as viewed from an altitude of 1000 m on 29 September and 25 November 1987.
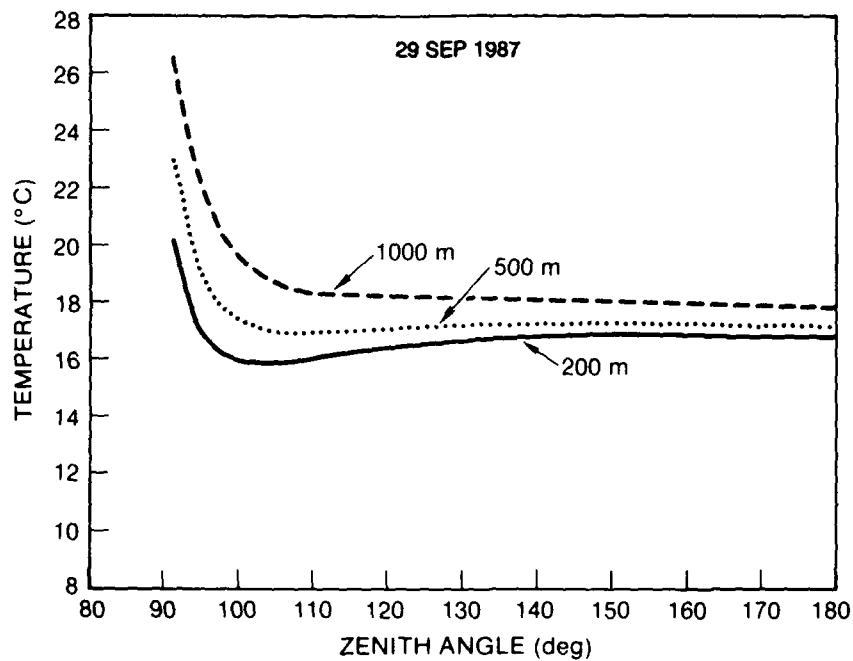

Figure 11. Calculations of the apparent blackbody temperature of the sea versus zenith angle as viewed from altitudes of 200 m, 500 m, and 1000 m on 29 September 1987.
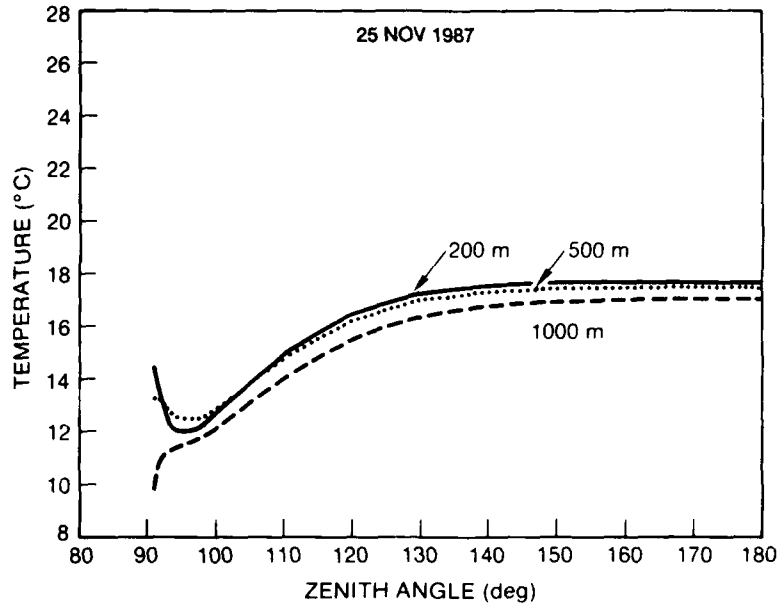
13

Figure 12. Calculations of the apparent blackbody temperature of the sea versus zenith angle as viewed from altitudes of 200 m, 500 m, and 1000 m on 25 November 1987.

position as the LOWTRAN calculations are iterated to determine the solution to the appropriate value of $\tau(R)$. The correct approach is to use the LOWTRAN code to directly calculate the sum of the target and path radiances received by the sensor at a range R as $N(R)_{t+p} = N(R = O)_t \tau(R) + N(R)_p$.

$N(R)_{t+p}$ is then converted to an equivalent blackbody temperature $T(R)_{t+p}$ by an iterative solution to Planck's blackbody formula. Similarly, an equivalent blackbody temperature, T_b, of the total background radiance (figure 12) at the specified range is calculated and the resulting apparent temperature difference, $\Delta T(R_a) = T(R)_{t+p} + T(R)_b$, determined. The intersection of the curves of $\Delta T(R)_a$ and the system's minimum detectable temperature difference (MDTD) plotted versus range will then determine the maximum detectable (MDR) of the target. In real-time situations, the amount of computer time required to determine the MDR, using an iteration technique, could be reduced considerably by search routines at specified zenith angles at each altitude.

REFERENCES

Cox, C., and W. Munk (1954). "Measurements of Roughness of the Sea Surface from Photographs of the Sun's Glitter," *Jour. Opt. Soc. of Am.*, 44, 838.

Griggs, M. (1975). "Measurements of Atmospheric Aerosol Thickness using ERTS-1 Data," *Jour. Air Pollut. Control Assoc.*, 25, 622.

Hughes, H. G. (1987). "Evaluation of the LOWTRAN 6 Navy Maritime Aerosol Model Using 8 to 12 μm Sky Radiances," *Opt. Eng.*, 26, 1155.

Kneizys, F. X., E. P. Shettle, W. O. Gallery, J. H. Chetwynd, Jr., J. H. Abreu, J. E. A. Selby, S. A. Clough, and R. W. Fenn (1983). *Atmospheric Transmittance/ Radiance: Computer Code LOWTRAN 6*. Air Force Geophysical Laboratory Technical Report No. 83–0187.

Wollenweber, F. G. (1988). *Effects of Atmospheric Model Layering on LOWTRAN 6 Calculations of 8 to 12 μm Near Horizon Sky Radiance*. NOSC TD 1193.

Wollenweber, F. G. (1988). *Infrared Sea Radiance Modeling Using LOWTRAN 6*. NOSC TD 1355.